

OPEN ACCESS

Electrochemical Deposition of Zero-Valent Iron from Alkaline Ceramic Suspensions of $\text{Fe}_{2-x}\text{Al}_x\text{O}_3$ for Iron Valorisation

To cite this article: Daniela V. Lopes *et al* 2020 *J. Electrochem. Soc.* **167** 102508

View the [article online](#) for updates and enhancements.



Electrochemical Deposition of Zero-Valent Iron from Alkaline Ceramic Suspensions of $\text{Fe}_{2-x}\text{Al}_x\text{O}_3$ for Iron Valorisation

Daniela V. Lopes,^{1,2,z} Andrei V. Kovalevsky,¹ Margarida J. Quina,² and Jorge R. Frade¹

¹CICECO—Aveiro Institute of Materials, Department of Materials and Ceramic Engineering, University of Aveiro, 3810-193 Aveiro, Portugal

²CIEPQPF—Research Centre on Chemical Processes Engineering and Forest Products, Department of Chemical Engineering, University of Coimbra, Rua Silvio Lima, 3030-790 Coimbra, Portugal

Electrochemical reduction of iron oxides into zero-valent iron (ZVI, Fe^0) is a promising alternative to the traditional methods used for iron production. The electrochemical deposition of Fe^0 from hematite and hematite-based $\text{Fe}_{2-x}\text{Al}_x\text{O}_3$ ceramic in alkaline suspensions (10 M of NaOH) was assessed at relatively low temperature (90 °C). Ceramic compositions aimed to mimic the main components of red mud waste from the alumina refining industry for iron valorisation purposes. The impact of aluminium content on the electroreduction and microstructure of the deposited Fe^0 films was demonstrated and discussed. Trapping and following the leaching of the aluminium species during deposition causes drastic morphological changes and induces significant porosity. Faradaic efficiencies of the reduction to Fe^0 were found to decrease from 70% to 32% for Fe_2O_3 and $\text{Fe}_{1.4}\text{Al}_{0.6}\text{O}_3$, respectively. The results highlight possible effects imposed by aluminium presence during Fe^0 electrodeposition for future iron recycling from, for example, red mud or other aluminium containing wastes by electrowinning in alkaline conditions.

© 2020 The Author(s). Published on behalf of The Electrochemical Society by IOP Publishing Limited. This is an open access article distributed under the terms of the Creative Commons Attribution Non-Commercial No Derivatives 4.0 License (CC BY-NC-ND, <http://creativecommons.org/licenses/by-nc-nd/4.0/>), which permits non-commercial reuse, distribution, and reproduction in any medium, provided the original work is not changed in any way and is properly cited. For permission for commercial reuse, please email: permissions@iopublishing.org. [DOI: [10.1149/1945-7111/ab9a2b](https://doi.org/10.1149/1945-7111/ab9a2b)]



Manuscript submitted March 16, 2020; revised manuscript received May 11, 2020. Published June 15, 2020.

Around 2 tons of CO_2 per ton of crude iron is generated by the traditional method of iron production in blast furnaces.^{1,2} Thus, low-temperature electrolysis-based processes for iron electrodeposition, have emerged as an alternative route for the direct conversion of iron oxide suspensions to metallic iron (Fe^0) without greenhouse gas emissions.^{1,3} Another potential advantage is that these processes may be integrated to balance intermittent energy supply by conversion of renewable energies into metal and possibly also storable gas by-products. Due to the relatively low operating temperatures (≤ 110 °C), this technology is gaining more attention when compared with others for iron production, such as molten oxide electrolysis^{4–6} or hydrogen flash smelting.^{7,8} The loop of different valence states of iron (Fe^{2+} and Fe^{3+}) between the cathode and the anode also prevents electrolysis in acid conditions. However, the Faradaic efficiencies of the process can be strongly affected by electrode overpotentials or current density and several other factors, such as the electrolyte concentration, solid load of iron oxide in suspension, temperature and stirring rate, mainly due to onset of hydrogen.^{9–11} On the other hand, the high hydrogen evolution observed in alkaline media can have an impact not only on the process efficiency but also on the porosity of Fe^0 deposits, leading to fragile structures.¹² To overcome this issue, around 18 M/19 M of an alkaline medium was frequently used as an electrolyte to suppress H_2 evolution near the working electrode.^{3,9,13–16} Strong alkaline electrolytes (≥ 12 M) lead to stable Faradaic efficiencies above 50% during the electrochemical reduction of Fe_2O_3 (50 g l^{-1}) in alkaline suspensions at 90 °C.¹³ More recently, about 70%–80% of current efficiency was achieved in 10 M alkaline suspensions of hematite¹⁰ and also in bulk hematite-based samples.¹⁷ However, the insulating nature of Fe_2O_3 still raises questions regarding its electroreduction mechanism. Some guidelines are provided by the results obtained in.¹⁷ In general, the works^{9,16–18} highlight the possibilities for the complete electrochemical reduction of bulk hematite, also pointing out the formation of Fe_3O_4 as an intermediate product. The use of compacted iron-containing ore as a cathode in the industry may represent a certain challenge due to insufficient electrical conductivity. On the other hand, other scenarios may exist where the electrochemical reduction of iron-containing suspensions can be rather relevant for the direct

processing of industrial slugs or iron oxide-rich wastes towards iron recycling.

Though iron oxides, namely hematite, are abundant as natural raw materials, some industrial wastes are also Fe-rich in iron oxides and must be treated or recycled to avoid serious environmental problems. A notorious example is the red mud alkaline waste from the alumina refining industry; this generates about 170 million tons annually,¹⁹ which requires specific treatment and disposal. The main components of red mud are Fe_2O_3 (>30 wt%), combined with aluminium oxide/oxyhydroxides, and many others (e.g. SiO_2 , CaO , Na_2O , and TiO_2).²⁰ Despite the complexity and diversity of red mud, iron recovery and recycling bring new perspectives for alumina and iron industries.

In addition to the huge scale of cast iron and steel production, it is important to note that zero-valent iron (Fe^0 , ZVI) has gained attention due to its reactivity ($E^0 = -0.44$ V for Fe^{2+} and $E^0 = -0.04$ V for Fe^{3+} , at 25 °C) to reduce a vast list of contaminants, including nitrate,²¹ Cr(VI),²² dyes from textile industries²³ and many other contaminants present in wastewaters²⁴ or in soils. Chemical^{25,26} and carbothermal²⁷ reductions are some of the most used methods for ZVI production, whereas electrochemical methods have been less studied as an alternative to process ZVI for environmental applications.

The present work challenges the electrodeposition of ZVI/ Fe^0 from alkaline hematite-based suspensions, mimicking the main components of the red mud waste for iron valorisation and ZVI production to reduce other pollutants. In this way, one used synthetic mixtures of known composition, to understand the impact of alumina, and to assess prospects to process ZVI by direct electrolysis of red mud, without or with minimum pre-treatments. For the sake of comparison, the ceramics with a nominal compositions $\text{Fe}_{2-x}\text{Al}_x\text{O}_3$ ($x = 0, 0.2, 0.6$) were processed in the same way as described in,²⁸ to result in highly porous materials with a cellular microstructure, which are further crushed into powder for the preparation of alkaline suspensions for the electroreduction studies. Particular novelty of this work includes the assessment of relevant effects imposed on the electroreduction process by the presence of aluminium oxide, as a main secondary component of the red mud waste.

Experimental

Hematite, Fe_2O_3 , and hematite-based cellular ceramic pieces, $\text{Fe}_{2-x}\text{Al}_x\text{O}_3$, with designed open porosity and with nominal compositions $\text{Fe}_{1.8}\text{Al}_{0.2}\text{O}_3$ and $\text{Fe}_{1.4}\text{Al}_{0.6}\text{O}_3$ were used as the precursors for the powder suspensions studied in the present work. The ceramic samples were processed with precise structural and microstructural characteristics by emulsification with liquid paraffin from powder suspensions containing Fe_2O_3 (Gute Chemie, abcr GmbH, 99.8%) and the corresponding amount of Al_2O_3 (Alcoa CT3000, 99.8%), as described elsewhere.²⁸ After emulsification and subsequent firing, all samples were crushed into powder ($<15\ \mu\text{m}$) for the preparation of suspensions. Pure hematite-based cellular ceramics were sintered in air at $1100\ ^\circ\text{C}$, while both $\text{Fe}_{1.8}\text{Al}_{0.2}\text{O}_3$ and $\text{Fe}_{1.4}\text{Al}_{0.6}\text{O}_3$ ceramics were fired at $1300\ ^\circ\text{C}$. All firing conditions involved similar heating and cooling rate of $3\ ^\circ\text{C}\ \text{min}^{-1}$ and $5\ ^\circ\text{C}\ \text{min}^{-1}$, respectively, and 2 h of dwell. The measurements of open porosity of the fired ceramic pieces were performed as described in.^{18,28,29} Particle size distributions of all the three crushed iron oxide compositions were studied with a Coulter LS 230 ($0.040\text{--}2000\ \mu\text{m}$).

A PTFE electrochemical cell filled with NaOH (100 ml, 10 M) electrolyte was used for the electrochemical studies. During the tests, the suspensions containing $67\ \text{g}\ \text{l}^{-1}$ of iron in the ceramic powder were stirred with a magnetic stirrer (100 rpm) to avoid sedimentation. The electrochemical reduction of the suspensions was performed at $90\ ^\circ\text{C}$. Platinum wire with a total area of $7.40\ \text{cm}^2$ in contact with the electrolyte was used as a counter electrode (CE), and Ni grid ($4.20\ \text{cm}^2$ exposed to the electrolyte, $0.90\ \text{mm}$ of aperture, $0.22\ \text{mm}$ of Ni wire diameter, $0.45\ \text{mm}$ of grid thickness) as a working electrode (WE), where the Fe^0 deposition occurred. The distance between CE and WE was $\approx 2.5\ \text{cm}$. The reference electrode (RE), $\text{Hg}|\text{HgO}|\text{NaOH}$ (1 M) ($+0.098\ \text{V}$ vs saturated hydrogen electrode), was connected by a Luggin capillary to the electrolyte. The electrochemical reduction studies were conducted using a VersaSTAT 4 (AMETEK) connected to the electrochemical cell; these included cyclic voltammetry (CV) starting from the open circuit potential (E_{OC}) in the range of $-1.2\ \text{V}$ to $0\ \text{V}$, with a scanning rate of $10\ \text{mV}\ \text{s}^{-1}$ and potentiostatic reduction to Fe^0 at $E = -1.08\ \text{V}$ for 7 h. After electrodeposition, Ni grids were washed with distilled water for NaOH removal and ethanol, and left for drying in a vacuum desiccator. Faradaic efficiencies of the processes were estimated by weighing the Ni grid before and after the electrochemical deposition of Fe^0 , which was then correlated with the total electric charge passed in the cell during the 7 h of the electrochemical process.

Microstructural studies were performed both for the ceramic pieces before crushing and for the Ni grids after the electrodeposition, using scanning electron microscopy (SEM), Hitachi SU-70 coupled with energy dispersive spectroscopy (EDS) analysis (Bruker Quantax 400 detector). Phase composition was assessed based on the results of X-ray diffraction (XRD) analysis, employing a PANalytical XPert PRO diffractometer ($\text{CuK}\alpha$ radiation, $2\theta = 10\text{--}80^\circ$) with a graphite monochromator. Phase identification was performed with Panalytical HighScore Plus 4.7 (PDF-4) software.

Results and Discussion

Structural and microstructural studies of ceramics and powdered samples.—The presence of specific microstructural features that may facilitate an electrochemical process, such as open porosity and interconnectivity of the pores, is essential for the electroreduction of iron-based bulk ceramics.^{17,18} While the larger pores are likely destroyed by the crushing procedure, the powder still can bear some inherent morphology of the parent ceramics. Porous structure also promotes comminution, with expected similar particle size and distribution in the resulting powder, if the same grinding procedure is applied for similar materials with comparable porosity. Figure 1 shows typical microstructures of the prepared ceramic samples, again confirming the feasibility of the used emulsification method for producing cellular ceramics. In previous work, Lopes et al.¹⁷

observed the collapse of $\text{Fe}_{1.8}\text{Al}_{0.2}\text{O}_3$ samples fired at $1100\ ^\circ\text{C}$ due to the high porosity level ($\approx 60\%$) and low mechanical strength inappropriate for the bulk electrochemical reduction. On the contrary, 100% of Fe^0 conversion was obtained for $\text{Fe}_{1.8}\text{Al}_{0.2}\text{O}_3$ bulk samples fired at $1300\ ^\circ\text{C}$ despite the lower open porosity level ($\approx 37\%$). Thus, in this work $\text{Fe}_{1.8}\text{Al}_{0.2}\text{O}_3$ and $\text{Fe}_{1.4}\text{Al}_{0.6}\text{O}_3$ samples were fired at $1300\ ^\circ\text{C}$ before being crushed into powder. On the other hand, Fe_2O_3 cellular pieces were sintered at $1100\ ^\circ\text{C}$ due to excessively high densification at $1300\ ^\circ\text{C}$ observed in.²⁸ As a result, the selected firing conditions allowed to produce comparable levels of porosity in the prepared materials within the range of 35%–49% (Table I).

XRD patterns (Fig. 1D) show segregation of a secondary Al_2O_3 -based phase only in the case of $\text{Fe}_{1.4}\text{Al}_{0.6}\text{O}_3$ composition, as observed for all firing temperatures range tested ($1100\text{--}1400\ ^\circ\text{C}$) in,²⁸ in fairly good agreement with the phase diagram.³⁰

Existing difference in the firing conditions for pure and Al-containing hematite does not affect significantly the particle size distribution (Fig. 2) of the powder after crushing, in accordance with the initial expectations based on comparable porosities. The average particle size corresponds to 5.1, 6.4 and $4.6\ \mu\text{m}$ for Fe_2O_3 , $\text{Fe}_{1.8}\text{Al}_{0.2}\text{O}_3$ and $\text{Fe}_{1.4}\text{Al}_{0.6}\text{O}_3$ compositions, respectively. The D_{50} size distribution curves show that 50% of particles have diameters lower than 3.9, 5.3 and $3.5\ \mu\text{m}$ for Fe_2O_3 , $\text{Fe}_{1.8}\text{Al}_{0.2}\text{O}_3$ and $\text{Fe}_{1.4}\text{Al}_{0.6}\text{O}_3$ samples. In all cases, D_{90} is lower than $15\ \mu\text{m}$.

Typical microstructures of powders obtained by crushing cellular ceramic samples are shown in Fig. 3. Though the designed porosity in the cellular ceramics is no longer present after crushing (Fig. 3A), larger particles still resemble the previous morphology (Fig. 3B).

Electrochemical reduction to ZVI.—The electrochemical processes occurring at the working electrode (WE) in the three alkaline suspensions were studied by cyclic voltammetry (CV). The corresponding curves show a sharp cathodic peak, and two diffuse broad peaks (Fig. 4). Hematite-based suspensions are known to have low electrical conductivity ($10^{-14}\ \text{s}\ \text{cm}^{-1}$)³¹ revealing low current densities and no electrochemical reactions prior the electrochemical deposition (image not shown). No noticeable contribution of the redox reaction involving nickel cations was observed during the CV analysis since anodic potentials higher than $0.30\ \text{V}$ are required for Ni oxidation.³² When testing a bulk $\text{Fe}_{1.8}\text{Al}_{0.2}\text{O}_3$ electrode in the same electrochemical conditions before amperometry analysis, Lopes et al.¹⁷ observed a cathodic peak (C) at $-0.97\ \text{V}$ and an anodic peak (A) at $-0.65\ \text{V}$. These peaks were related to a minor reduction of $\text{Fe}_{1.8}\text{Al}_{0.2}\text{O}_3$ to Fe_3O_4 , and consequently, to Fe(II) (C); and a minor oxidation of Fe(II) species to FeOOH and/or Fe_3O_4 (A). However, in the cited work a direct electrical contact between the ceramic $\text{Fe}_{1.8}\text{Al}_{0.2}\text{O}_3$ cathode and a nickel foil was provided by a silver paste, leading to a noticeable contribution of the redox reactions involving iron even prior to the electroreduction, highlighting principal differences of these approaches. A sharp current increase at cathodic potentials below $-1.10\ \text{V}$ can be attributed to the start of hydrogen evolution.^{10,17}

After 7 h of Fe^0 electrodeposition, an intense peak (C) is present at $\approx -1.086\ \text{V}$ for Fe_2O_3 and $-1.071\ \text{V}$ for $\text{Fe}_{1.4}\text{Al}_{0.6}\text{O}_3$ (Fig. 4). At the same potentials, no peak was present in¹⁷ for bulk samples of $\text{Fe}_{1.8}\text{Al}_{0.2}\text{O}_3$ after electroreduction. However, one should notice that this cathodic peak lies in the range of the potentials which correspond to C_2 observed in¹⁷ and thus, likely, corresponds to complete reduction to Fe^0 . As an example, an onset potential at $-1.1\ \text{V}$ (vs $\text{Hg}|\text{HgO}$) was attributed to a simultaneous Fe(II) reduction to Fe^0 and H_2 evolution in similar experimental conditions in¹⁰; a peak at $-1.06\ \text{V}$ (vs $\text{Hg}|\text{HgO}$) was associated with reduction to Fe^0 ¹; and an onset potential of $-1.1\ \text{V}$ evolving to a peak reaching a maximum at $-1.13\ \text{V}$ was attributed to the reduction to Fe^0 in.³³ The reduction of Fe(III) to Fe(II) species (e.g. Fe(OH)_3^- , HFeO_2^-) usually involves Fe_3O_4 as an intermediate phase, as previously demonstrated in bulk electroreduction.^{9,15,17,18} However, in opposition to the latter case where the whole WE is

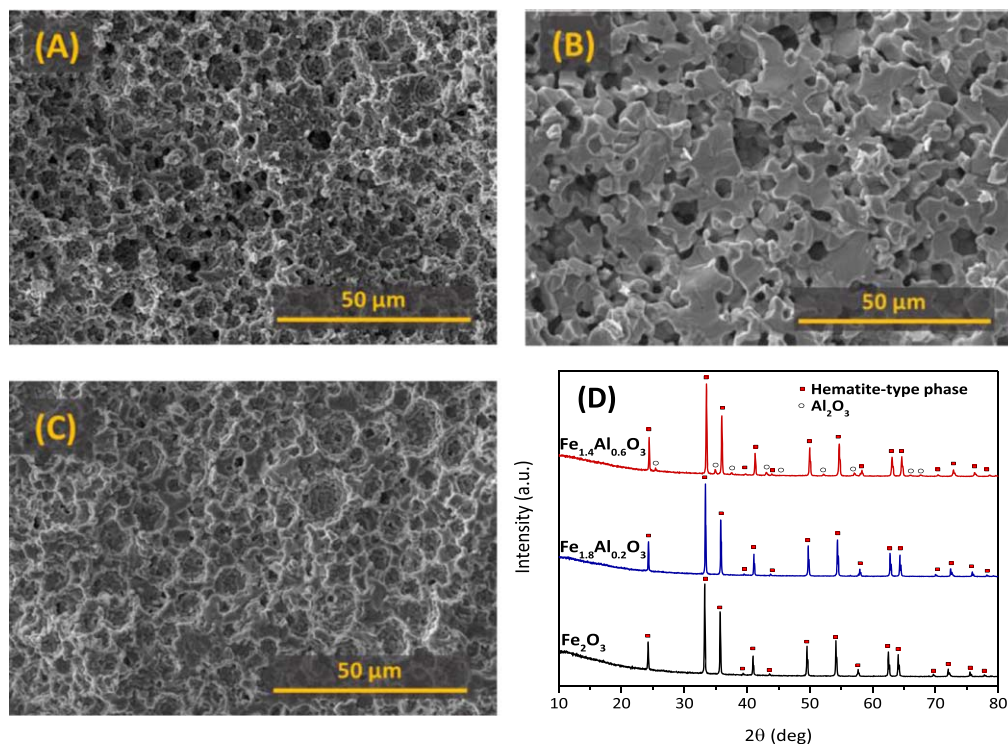


Figure 1. SEM images of the fractured cellular ceramics: (A) Fe_2O_3 (1100 °C), (B) $\text{Fe}_{1.8}\text{Al}_{0.2}\text{O}_3$ (1300 °C), (C) $\text{Fe}_{1.4}\text{Al}_{0.6}\text{O}_3$ (1300 °C); (D) corresponding XRD patterns.

Table I. Firing conditions and open porosities (x_0) of $\text{Fe}_{2-x}\text{Al}_x\text{O}_3$ cellular ceramics.

Nominal composition	T_{firing} (°C)	x_0
Fe_2O_3	1100	0.47 ± 0.04
$\text{Fe}_{1.8}\text{Al}_{0.2}\text{O}_3$	1300	0.35 ± 0.02
$\text{Fe}_{1.4}\text{Al}_{0.6}\text{O}_3$	1300	0.49 ± 0.02

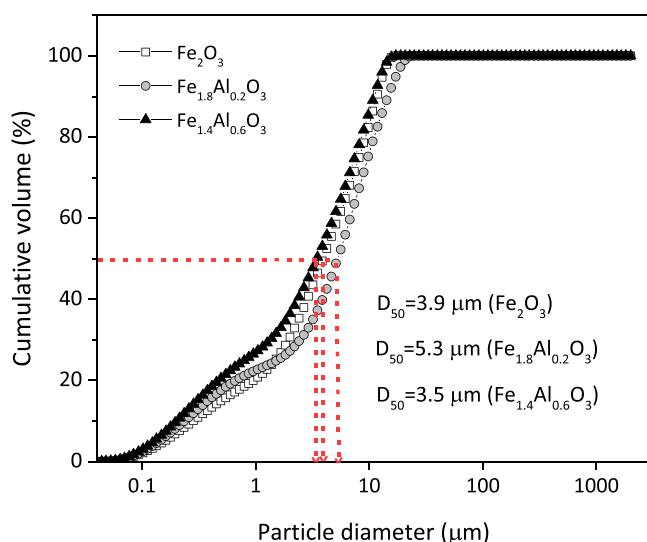


Figure 2. Size distribution of the powder after crushing.

composed of a $\text{Fe}_2\text{O}_3/\text{Fe}_3\text{O}_4/\text{Fe}$ composite, the electrode in the present work after suspension electroreduction represents a metallic iron layer deposited on the nickel plate, presumably with a thin oxidised layer at the surface. Thus, the cathodic peaks corresponding

to the formation of Fe_3O_4 and Fe(II) species might not be easily observed by cyclic voltammetry in this work. The high conductivity of Fe_3O_4 ($\approx 10^2$ to 10^3 s cm^{-1})⁵¹ may facilitate its fast conversion to Fe^0 at the surface of the electrodeposited layer.

On sweeping the potential (Fig. 4), anodic peaks at $\approx -0.882 \text{ V}$ (A_1) and $\approx -0.570 \text{ V}$ (A_2) are essentially similar to those reported earlier for bulk electrodes,¹⁷ and can be attributed to the oxidation of Fe^0 to Fe(II) species and, subsequently, its oxidation to FeOOH and/or Fe_3O_4 . The area of A_2 peak noticeably decreases for the higher content of aluminium. Somewhat similar redox stabilisation effect of Al^{3+} addition on 2+ oxidation state of iron oxides was previously demonstrated for aluminium-containing ferrosinels.^{34,35}

Figure 4 also shows sharp decay of the cathodic peak at the onset of intensive hydrogen evolution, allowing one to de-convolute these processes and to compute the stored charge ascribed to the reduction to Fe^0 (Q_{Fe}) as shown in Fig. 5, where j represents the current density in mA cm^{-2} . The hydrogen evolution current density, j_{H_2} , was extrapolated to obtain $j_{\text{Fe}} = j - j_{\text{H}_2}$, and the corresponding stored charge ascribed to the reduction to Fe^0 was computed by the integration of the current density (Eq. 1):

$$Q_{\text{Fe}} = \int j_{\text{Fe}} dt = \frac{1}{\beta} \int_{E_{\text{on}}}^{E_d} (j - j_{\text{H}_2}) dE \quad [1]$$

where the scan rate $\beta = dE/dt$ allows the transformation of time scale to potential $dt = dE/\beta$. Thus, an alternative representation of cyclic voltammograms (j/β vs E) is shown in Fig. 5, for a ready analysis of the stored charge, based on the cathodic peak area, integrated between the limiting values of onset and decay potentials (E_{on} and E_d). These results are summarized in Table II, to emphasize not only the effects of alumina on the Fe^0 deposition, as revealed by the corresponding stored charge (Q_{Fe}), but also the effects on hydrogen evolution at decay potential of Fe^0 -reduction. Thus, increasing the alumina content in the solid load of suspensions hinders the reduction to Fe^0 , with high correlation ($R^2 = 0.999$), as well as between alumina content and current density of hydrogen evolution, $j_{\text{H}_2,d}$, at the decay potential, E_d ($R^2 = 0.994$). This

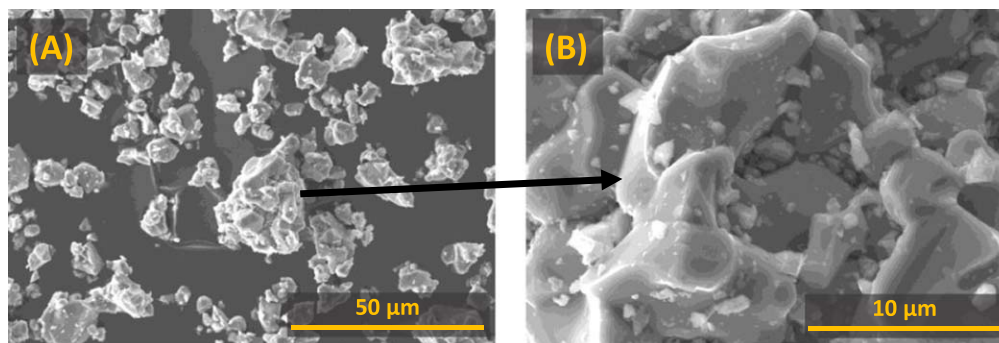


Figure 3. Powders of $\text{Fe}_{2-x}\text{Al}_x\text{O}_3$ processed ceramics after crushing (A) general view and (B) walls of a previous cavity cell.

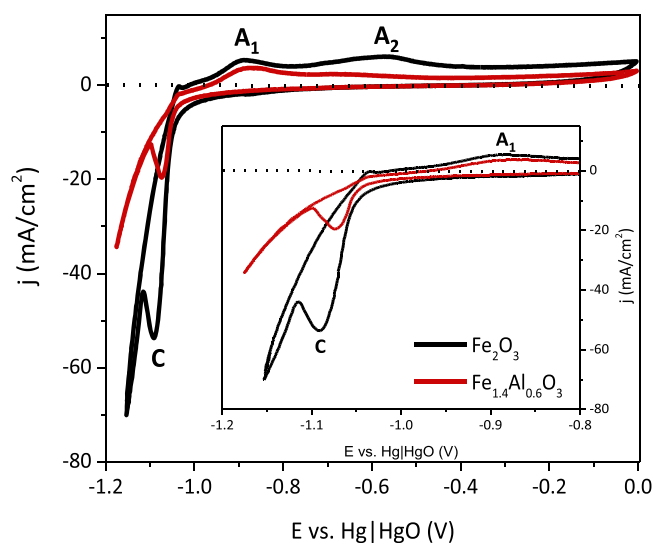


Figure 4. Cyclic voltammetry performed at 0.01 V s^{-1} after 7 h of Fe^0 deposition from suspensions of Fe_2O_3 (black line) and $\text{Fe}_{1.4}\text{Al}_{0.6}\text{O}_3$ (red line). The insert image shows expanded scales of the main cathodic and anodic peaks.

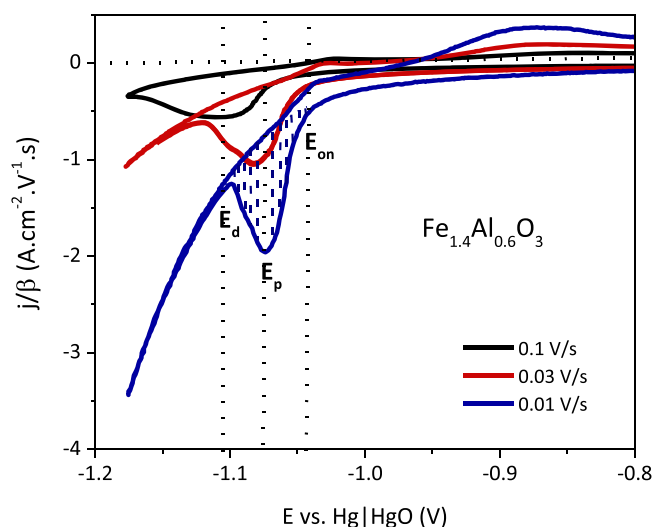


Figure 5. Cyclic voltammograms of $\text{Fe}_{1.4}\text{Al}_{0.6}\text{O}_3$ suspensions at different scan rates. The shaded area represents the stored charge of the cathodic peak per unit area.

indicates that the fraction of alumina in the $\text{Fe}_{2-x}\text{Al}_x\text{O}_3$ suspensions sets similar inhibitions on Fe^0 -deposition and H_2 evolution, probably by partial coverage of the conducting Fe^0 surface with insulating

alumina-based deposits, as it will be shown later. Note also that the values of decay potential shown in Table II are still insufficient to reduce trivalent aluminium species such as AlO_2^- to Al^0 .³⁶

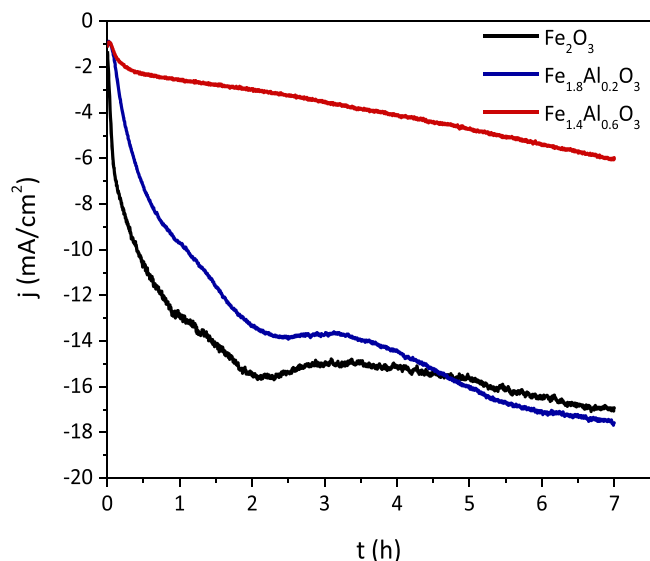
Figure 5 also shows that by increasing the scan rates, a shift on the cathodic peak of reduction to Fe^0 can be observed as well as a shift on the hydrogen evolution to higher cathodic polarizations. This is also revealed by the correlations between the peak potential and scan rate ($R^2 = 0.996$) and the correlation between the decay potential and scan rate ($R^2 = 0.988$). In addition, the stored charge varies inversely with the hydrogen current density at the decay potential ($Q_{\text{Fe}} \text{ vs } 1/j_{\text{H}_2, \text{on}}$ with $R^2 = 0.991$). Thus, higher scan rates shift the operating conditions to higher cathodic polarization, and change the interplay between hydrogen evolution and Fe^0 -deposition, probably because H_2 bubbles restrict the contacts of $\text{Fe}_{2-x}\text{Al}_x\text{O}_3$ particles with the conducting Fe^0 -layer, and possibly also because a slight overpressure contributes to detachments of loosely bond Fe^0 -crystals from highly porous Fe^0 -deposits. In fact, it is well known that Faradaic efficiencies of the electrodeposition process decreases significantly when the WE is polarized from -1.09 V (vs $\text{Hg}|\text{HgO}$) to higher cathodic polarizations,³⁷ promoting the hydrogen evolution reaction ($2\text{H}_2\text{O} + 2e^- \rightarrow \text{H}_2 + 2\text{OH}^-$), where the formation of Fe^0 competes with H_2 release, resulting in an overlapped shoulder in the CV.

Electrodeposition tests were performed for 7 h at -1.08 V in potentiostatic mode (Fig. 6), showing an increase in the cathodic current density with time for all samples. In general, the increase in the cathodic current can be ascribed to an increase in the effective area of the electrode, based on nearly cylindrical symmetry of the deposited Fe^0 layer, and probably its high porosity. These results can be compared to those obtained for bulk hematite-based cathodes, tested under similar conditions.¹⁷ Despite the low conductivity of hematite-based materials, once the first Fe_3O_4 and/or Fe^0 crystals are formed in bulk electrode, the reaction is further boosted by these new conductive pathways. In the case of suspension, each particle reacts separately, while a gradual current increase is actually provided by an increase in the cathode area with time, as discussed below.

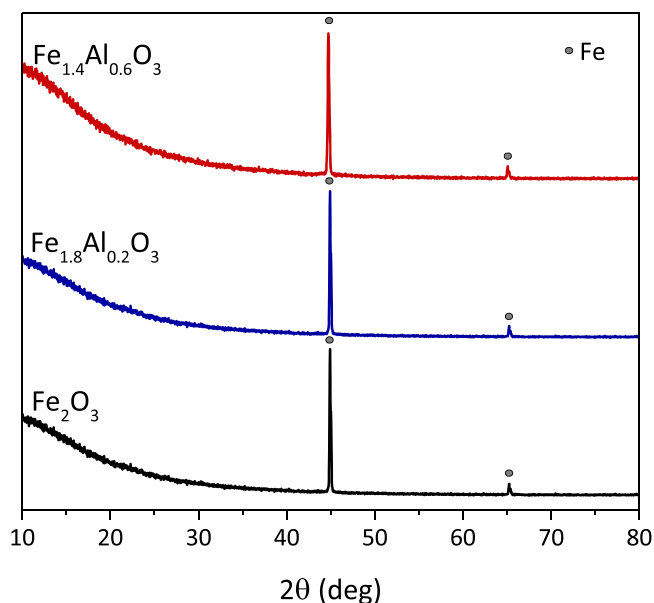
The same potential was applied during the bulk reduction of $\text{Fe}_{1.8}\text{Al}_{0.2}\text{O}_3$ to Fe^0 in¹⁷ for comparison purposes, where close to 100% of $\text{Fe}(\text{III})$ conversion to Fe^0 was obtained. However, this may not be the case in the present study, as illustrated by extrapolating the hydrogen evolution current density (Fig. 5). The time dependence in Fig. 6 may also comprise enhanced hydrogen evolution, mainly for conditions when the deposited Fe^0 -layers are highly porous. This is confirmed by the limited Faradaic efficiencies of 70%, 55% and 32%, estimated for Fe^0 -deposition from suspensions of Fe_2O_3 , $\text{Fe}_{1.8}\text{Al}_{0.2}\text{O}_3$ and $\text{Fe}_{1.4}\text{Al}_{0.6}\text{O}_3$, respectively. Note that literature studies report efficiencies in the range of 70%–94%^{3,14,33} for Fe_2O_3 suspensions with 18 M of NaOH as an electrolyte and at $110 \text{ }^\circ\text{C}$ – $114 \text{ }^\circ\text{C}$, with different CEs and WEs. Nevertheless, some results obtained in the present study, for the reference Fe_2O_3 suspension, may be explained by significant differences in operating conditions, namely the use of 10 M electrolyte concentration and 90

Table II. Onset potential (E_{on}); peak potential (E_p); decay potential (E_d); stored charge of the Fe^0 -deposition peak (Q_{Fe}) and estimated current density of hydrogen evolution at the decay potential ($j_{H_2,on}$).

	β ($V s^{-1}$)	E vs Hg HgO (V)			Q_{Fe} ($C cm^{-2}$)	$j_{H_2,on}$ ($mA cm^{-2}$)
		E_{on}	E_p	E_d		
Fe_2O_3	-0.01	-1.051	-1.086	-1.115	-0.093	-44
$Fe_{1.8}Al_{0.2}O_3$	-0.01	-1.057	-1.090	-1.123	-0.076	-36
$Fe_{1.4}Al_{0.6}O_3$	-0.01	-1.042	-1.073	-1.104	-0.039	-13
"	-0.03	-1.040	-1.083	-1.126	-0.032	-18
"	-0.1	-1.047	-1.109	-1.171	-0.023	-34

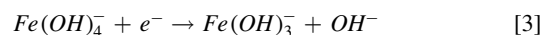
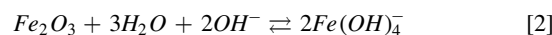
**Figure 6.** Current vs time curves of Fe^0 electrodeposition from Fe_2O_3 , $Fe_{1.8}Al_{0.2}O_3$ and $Fe_{1.4}Al_{0.6}O_3$ suspensions at -1.08 V (90 °C, NaOH 10 M).

°C when compared to 18 M and higher temperatures in earlier studies, to minimize the impact of H_2 evolution.¹⁴ Nevertheless, much lower Faradaic efficiency was obtained for the deposition of

**Figure 7.** XRD patterns of Ni grids after Fe^0 deposition from Fe_2O_3 , $Fe_{1.8}Al_{0.2}O_3$ and $Fe_{1.4}Al_{0.6}O_3$ suspensions.

Fe^0 from suspensions of $Fe_{1.8}Al_{0.2}O_3$ and $Fe_{1.4}Al_{0.6}O_3$, confirming the negative impact of increasing fractions of alumina.

The mechanism of the Fe_2O_3 electroreduction in alkaline suspensions is still uncertain in literature. The solubility of hematite and hematite-based suspensions in 10 M of NaOH, 90 °C should only be slightly higher than 1.1×10^{-3} M (76 °C, 10 M).³⁸ Despite the low solubility, the conversion of Fe_2O_3 to $Fe(OH)_4^-$ has been proposed as a relevant step of Fe^0 -electrowinning in alkaline suspensions,^{3,14,33,39} as described by Eq. 2, and thermodynamic studies considered the hydrolysis of Fe_2O_3 to form $Fe(OH)_4^-$.⁴⁰ The $Fe(OH)_4^-$ anions might be reduced to Fe(II) species, mainly as $Fe(OH)_3^-$ (Eq. 3), which is further electroreduced and deposited in the WE as Fe^0 (Eq. 4).



However, the contribution of such mechanism may be limited due to the low solubility of Fe_2O_3 particles. As an alternative, one can consider the electroreduction mechanism described for bulk electrolysis,^{16–18} including the following steps: $Fe_2O_3 \rightarrow Fe_3O_4 \rightarrow Fe(II) \rightarrow Fe^0$. An electroreduction mechanism based on the adsorption of Fe_2O_3 particles in contact with WE has been proposed by Siebentritt and his co-workers.³⁹ Though negative charge on the surface of Fe_2O_3 particles should be expected at strong alkaline conditions, since the isoelectric point (IEP) of hematite is in the pH range of 6–9.6, zeta potential measurements by electroacoustic methods³⁹ indicated a transition from negative to slightly positive values for 0.1 M to 10 M NaOH solution, respectively. In this case, positive charge by Na^+ cations, surrounding the hematite particles, may promote their migration towards the cathodically polarized WE by electrostatic forces. Thus, one may consider a combination of the stated mechanisms above to the electroreduction of Fe_2O_3 . For the reasons described above, the cathodic peak which corresponds to Fe(III) to Fe(II) reduction may be hidden.

The current densities in Fig. 6 remain below -18 mA cm^{-2} even for electrodeposition from Fe_2O_3 suspension. These results are clearly lower than reported in previous studies, with up to 100 mA cm^{-2} in some cases.^{14,33} However, more concentrated electrolyte solution and higher process temperature (110 °C– 114 °C) were used in the cited work and both factors are expected to facilitate the electroreduction. In addition, the irregular shape of Fe_2O_3 particles obtained by grinding the precursor cellular ceramics (Fig. 3) may impose stereological restrictions on the contacts of particles with the current collecting Fe^0 -surface.

The XRD results in Fig. 7 confirm the formation of pure Fe^0 at the cathode for all studied suspensions, without any evidence of non-metallic inclusions, and possibly with preferential orientation. This is consistent with the characteristic morphology of Fe^0 crystals deposited on the Ni grid during the electrochemical reduction of Fe_2O_3 -based suspensions (Fig. 8), growing in columnar shape

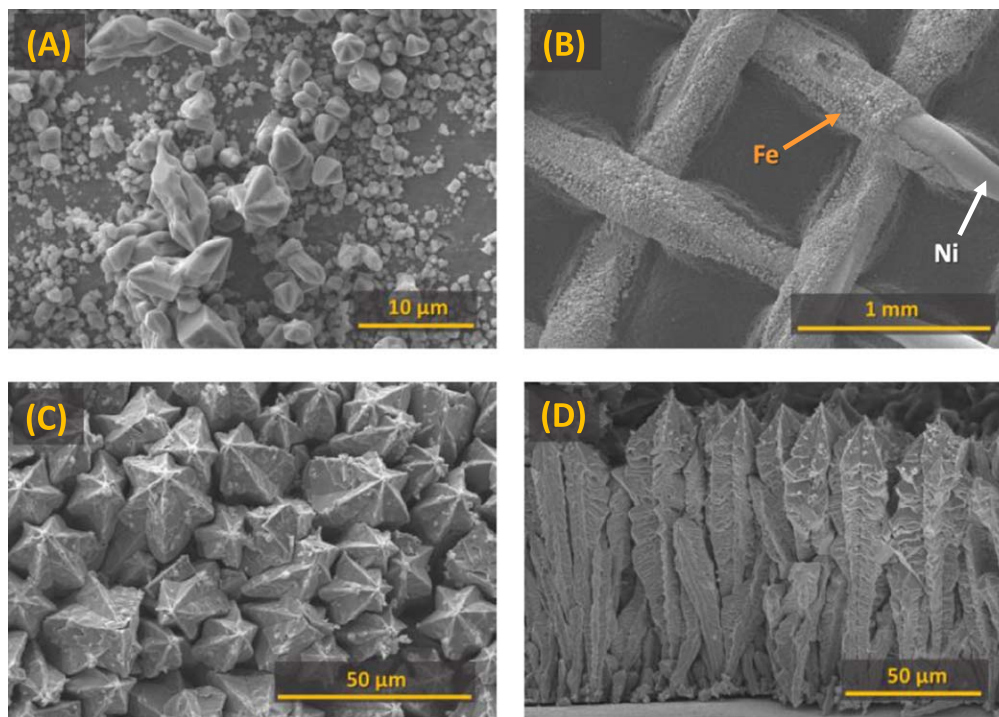
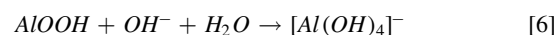
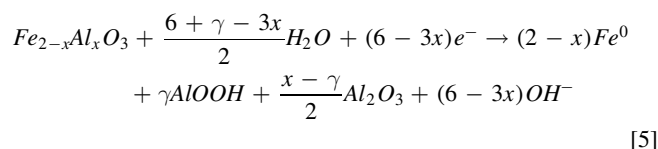


Figure 8. Microstructural evolution of Fe^0 crystals deposited during (A) 20 min; (B), (C) and (D) 7 h of electroreduction of Fe_2O_3 -based suspensions, where (B) shows the Ni grid covered by Fe^0 crystals, while (C) represents a top view of Fe^0 crystals and (D) a side view.

($\approx 18 \mu\text{m}$ of diameter). After 20 min of electroreduction, the smaller crystals evolve by growing on the top of previous nuclei (Fig. 8A). Columnar Fe^0 crystals grow perpendicularly to the Ni grid; the contrast between the layer of Fe^0 crystals and the Ni grid is well visible in Fig. 8B. After 7 h of electrodeposition, compact needle-like or dendritic crystals with $\approx 108 \mu\text{m}$ of length (Figs. 8C, 8D) can be observed, similar to those observed in.¹⁴

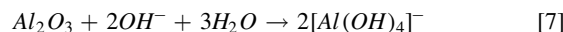
Such dendritic morphology of the Fe^0 deposits is retained for all the alkaline suspensions tested (Fig. 9). Differences in morphology are likely provided by higher current densities observed for Fe_2O_3 containing suspension at the initial stage, which largely determines the landscape of the crystallite. However, these microstructures also mark a tendency to form smaller dendrites for a larger content of aluminium in the $\text{Fe}_{2-x}\text{Al}_x\text{O}_3$ suspension (Figs. 9A, 9B), finally resulting in entirely distinct morphology observed for the $\text{Fe}_{1.4}\text{Al}_{0.6}\text{O}_3$ suspension (Figs. 9C, 9D). Fe^0 dendrites electrodeposited from $\text{Fe}_{1.4}\text{Al}_{0.6}\text{O}_3$ suspensions (Figs. 9C, 9D) appear to be thinner ($\approx 13 \mu\text{m}$) and highly-porous, with an asymmetrical growth and shape. The high porosity shown in Fig. 9D is likely promoted by surface coverage by Al-rich precipitates, which may correspond to Al_2O_3 , AlOOH and $\text{Na}[\text{Al}(\text{OH})_4]$ species or mixture thereof. Note that these inclusions are barely observed after Fe^0 -electrowinning from $\text{Fe}_{1.8}\text{Al}_{0.2}\text{O}_3$, which proved to be single-phase (Fig. 1D). Thus, one may assume that the extent of surface coverage by the alumina-rich precipitates is dictated mainly by the excess of alumina, present as a secondary corundum-based phase in the precursor powders with nominal composition $\text{Fe}_{1.4}\text{Al}_{0.6}\text{O}_3$, rather than by segregation of the alumina content dissolved in the hematite phase, during its electroreduction. Partial coverage of the current collecting and electrochemically active Fe^0 -surface by those Al-rich precipitates may explain simultaneous effects on Fe^0 -electrowinning and on hydrogen evolution, as described above.

Thus, the corresponding reactions of cathodic iron reduction, accompanied with aluminium redistribution, can be presented as follows (Eqs. 5–6):



where γ represents the fraction of AlOOH formed.

Simultaneously, the highly alkaline electrolyte may still promote dissolution of the corundum phase:



which may also explain the corresponding porosity in the dendrites, observed mainly for Fe^0 -deposition from $\text{Fe}_{1.4}\text{Al}_{0.6}\text{O}_3$ (Fig. 9D). In addition, this may also contribute to enhance the relative contribution of hydrogen evolution at the inner porosity of Fe^0 -based electrodes,⁴¹ whereas Fe^0 -electrodeposition may be limited to the outermost surface of the Fe^0 -layer.

The obtained results generally suggest that the presence of aluminium in red mud is not expected to be a decisive obstacle towards the electrochemical reduction in suspensions with low Al content, but may significantly determine the microstructure of the produced ZVI, while also impairing the electroreduction current and Faradaic efficiency. On the other hand, the presence of high concentrations of Al may have a direct impact on the electroreduction pathway. In fact, the addition of 30 wt% of kaolinite ($\text{Al}_2\text{Si}_2\text{O}_5(\text{OH})_4$) in Fe_2O_3 alkaline suspension, was responsible for lowering the Faradaic efficiency from 80% (0 wt% of kaolinite) to 38%, due to the possible phase formations of cancrinite or sodalite at the surface of hematite particles, hampering the electroreduction in.⁴² At the same time, gradual leaching of aluminium-containing species may create additional flexibility for the functional design of the deposited films. Firstly, the dissolution rate can be adjusted by pH and the temperature of the electrolyte, to compensate for the formation of excessive porosity in the dendrites during fast film

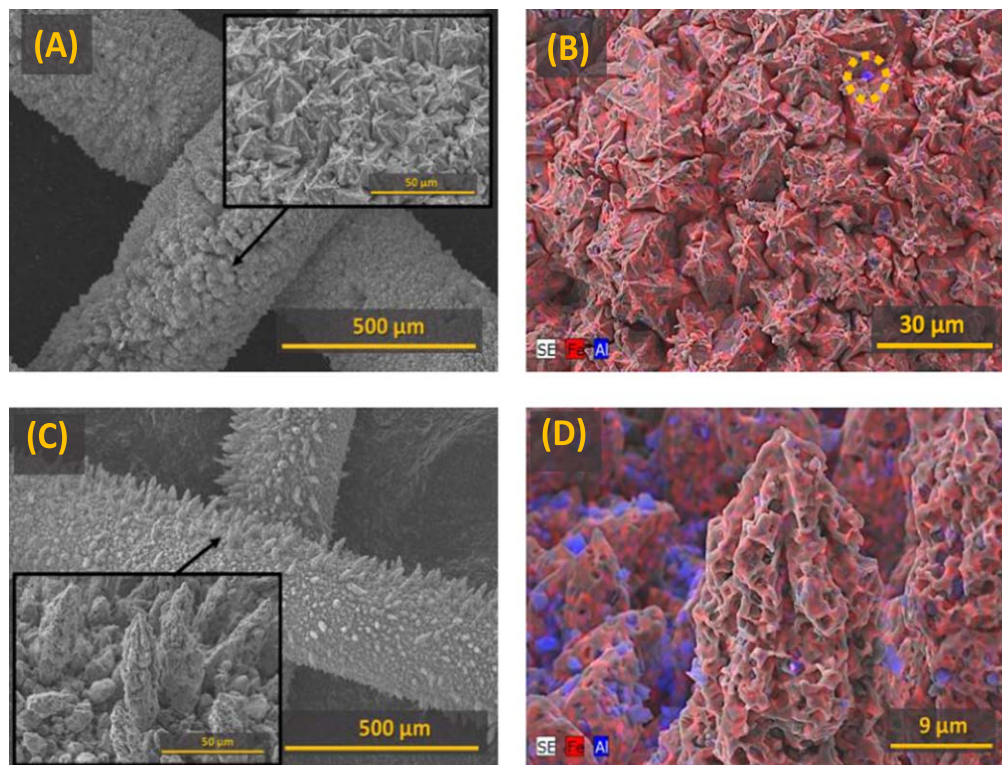


Figure 9. SEM images of Fe^0 crystals after electrochemical reduction of suspensions containing (A) and (B) $\text{Fe}_{1.8}\text{Al}_{0.2}\text{O}_3$; (C) and (D) $\text{Fe}_{1.4}\text{Al}_{0.6}\text{O}_3$. Images (B) and (D) show EDS mappings.

growth. Secondly, the controlled formation of the porosity may be even favourable for potential environmental applications of ZVI, where high surface area is often required. Thus, although these guidelines were obtained for synthetic compositions mimicking the main components of the red mud, they are still expected to contribute to the understanding of prospective conditions and possible outcomes for the process of the electrochemical reduction of iron-containing ores and industrial slugs.

Conclusions

Electrochemical reduction of hematite and hematite-based ($\text{Fe}_{2-x}\text{Al}_x\text{O}_3$) ceramic suspensions to zero-valent iron (ZVI, Fe^0) was assessed in strong alkaline conditions at relatively low temperature ($90\text{ }^\circ\text{C}$) and proved to be feasible. Microstructural studies have shown that electrodeposition results in the formation of Fe^0 films having a columnar dendritic structure. The presence of alumina was found to affect the morphology of the dendrites and to promote the formation of significant porosity in crystallites when performing the electrodeposition from $\text{Fe}_{1.4}\text{Al}_{0.6}\text{O}_3$. This porosity is believed to result from mechanical trapping of the aluminium-rich species in the Fe^0 films during growth, followed by their dissolution promoted by highly-alkaline electrolytes. Increasing the aluminium content in suspensions depressed the electroreduction current and also affected the Faradaic efficiency of the electrodeposition from 70% (Fe_2O_3), 55% ($\text{Fe}_{1.8}\text{Al}_{0.2}\text{O}_3$) to 32% ($\text{Fe}_{1.4}\text{Al}_{0.6}\text{O}_3$), probably because partial surface coverage with alumina-based precipitates affects interactions of hematite-based particles with the current collecting Fe^0 -layer. Nevertheless, the results have demonstrated that the electrochemical deposition of Fe^0 may be a feasible process for iron recovery and recycling from aluminium-containing wastes, such as red mud.

Acknowledgments

The carried research was supported by the FCT grant PD/BD/114106/2015, the European Commission (project SIDERWIN-DLV-768788-Horizon 2020/SPIRE10) and the project CICECO-

Aveiro Institute of Materials (ref. UIDB/50011/2020 and UIDP/50011/2020), financed by the COMPETE 2020 Program and National Funds through the FCT/MEC and when applicable co-financed by FEDER under the PT2020 Partnership Agreement.

ORCID

Daniela V. Lopes <https://orcid.org/0000-0003-0652-5070>
 Andrei V. Kovalevsky <https://orcid.org/0000-0001-5814-9797>
 Margarida J. Quina <https://orcid.org/00-0002-9651-2427>
 Jorge R. Frade <https://orcid.org/0000-0001-8445-2562>

References

- Q. Wang, Y. Zhu, Q. Wu, E. Gratz, and Y. Wang, *RSC Adv.*, **5**, 5501 (2015).
- E. A. Mousa, *Metall. Mater. Eng.*, **25**, 69 (2019).
- A. Allanore, H. Lavelaine, G. Valentin, J. P. Birat, and F. Lapique, *J. Electrochem. Soc.*, **154**, E187 (2007).
- D. R. Sadoway, *J. Mater. Res.*, **10**, 487 (1995).
- H. Kim, J. Paramore, A. Allanore, and D. R. Sadoway, *J. Electrochem. Soc.*, **158**, E101 (2011).
- A. Allanore, *J. Electrochem. Soc.*, **162**, E13 (2015).
- M. Y. Mohassab-Ahmed, H. Y. Sohn, and H. G. Kim, *Ind. Eng. Chem. Res.*, **51**, 3639 (2012).
- H. K. Pinegar, M. S. Moats, and H. Y. Sohn, *Ironmak. Steelmak.*, **40**, 44 (2013).
- A. Allanore, H. Lavelaine, G. Valentin, J. P. Birat, and F. Lapique, *J. Electrochem. Soc.*, **155**, E125 (2008).
- Y. A. Ivanova, J. F. Monteiro, A. L. Horovitz, D. K. Ivanou, D. Mata, R. F. Silva, and J. R. Frade, *J. Appl. Electrochem.*, **45**, 515 (2015).
- J. F. Monteiro, Y. A. Ivanova, A. V. Kovalevsky, D. K. Ivanou, and J. R. Frade, *Electrochim. Acta*, **193**, 284 (2016).
- B. Yuan and G. M. Haarberg, *ECS Trans.*, **16**, 31 (2009).
- J. A. M. LeDuc, R. E. Lofffield, and L. E. Vaaler, *J. Electrochem. Soc.*, **106**, 659 (1959).
- B. Yuan, O. E. Kongstein, and G. M. Haarberg, *J. Electrochem. Soc.*, **156**, D64 (2009).
- A. Allanore, H. Lavelaine, G. Valentin, J. P. Birat, P. Delcroix, and F. Lapique, *Electrochim. Acta*, **55**, 4007 (2010).
- X. Zou, S. Gu, X. Lu, X. Xie, C. Lu, Z. Zhou, and W. Ding, *Metall. Mater. Trans. B*, **46B**, 1262 (2015).
- D. V. Lopes, Y. A. Ivanova, A. V. Kovalevsky, A. R. Sarabando, J. R. Frade, and M. J. Quina, *Electrochim. Acta*, **327**, 135060 (2019).

18. Y. A. Ivanova, J. F. Monteiro, L. B. Teixeira, N. Vitorino, A. V. Kovalevsky, and J. R. Frade, *Mater. Des.*, **122**, 307 (2017).
19. Y. Hua, K. V. Heal, and W. Friesl-Hanl, *J. Hazard. Mater.*, **325**, 17 (2017).
20. M. A. Khairul, J. Zanganeh, and B. Moghtaderi, *Resour. Conserv. Recycl.*, **141**, 483 (2019).
21. Y. Liu and J. Wang, *Sci. Total Environ.*, **671**, 388 (2019).
22. C. Mystrioti, D. Sparis, N. Papasiopi, A. Xenidis, D. Dermatas, and M. Chrysochoou, *Bull. Environ. Contam. Toxicol.*, **94**, 302 (2015).
23. C. Raman and S. Kanmani, *J. Environ. Manag.*, **177**, 341 (2016).
24. R. C. Martins, D. V. Lopes, M. J. Quina, and R. M. Quinta-ferreira, *Chem. Eng. J.*, **192**, 219 (2012).
25. C. B. Wang and W. X. Zhang, *Environ. Sci. Technol.*, **31**, 2154 (1997).
26. J. T. Nurmi et al., *Environ. Sci. Technol.*, **39**, 1221 (2005).
27. M. Bystrzejewski, *J. Solid State Chem.*, **184**, 1492 (2011).
28. D. V. Lopes, A. V. Kovalevsky, M. J. Quina, and J. R. Frade, *Ceram. Int.*, **44**, 20354 (2018).
29. S. W. Hughes, *Phys. Educ.*, **40**, 468 (2005).
30. M. Maruyama, T. Fukasawa, S. Suenaga, and Y. Goto, *J. Eur. Ceram. Soc.*, **24**, 463 (2004).
31. K. K. Lee, S. Deng, H. M. Fan, S. Mhaisalkar, H. R. Tan, E. S. Tok, K. P. Loh, W. S. Chin, and C. H. Sow, *Nanoscale*, **4**, 2958 (2012).
32. J. M. Skowroński, T. Rozmanowski, and M. Osińska, *Process Saf. Environ. Prot.*, **93**, 139 (2015).
33. V. Feynerol, H. Lavelaine, P. Marlier, M. N. Pons, and F. Lapicque, *J. Appl. Electrochem.*, **47**, 1339 (2017).
34. A. V. Kovalevsky, E. N. Naumovich, A. A. Yaremchenko, and J. R. Frade, *J. Eur. Ceram. Soc.*, **32**, 3255 (2012).
35. A. V. Kovalevsky, A. A. Yaremchenko, E. N. Naumovich, N. M. Ferreira, S. M. Mikhalev, F. M. Costa, and J. R. Frade, *J. Eur. Ceram. Soc.*, **33**, 2751 (2013).
36. M. Pourbaix, *Atlas of Electrochemical Equilibria in Aqueous Solutions* (National Association of Corrosion Engineers) 2nd ed. (Houston, Texas) p. 644 (1974).
37. P. Periasamy, B. R. Babu, and S. V. Iyer, *J. Power Sources*, **63**, 79 (1996).
38. K. Ishikawa, T. Yoshioka, T. Sato, and A. Okuwaki, *Hydrometallurgy*, **45**, 129 (1997).
39. M. Siebentritt, P. Volovitch, K. Ogle, and G. Lefèvre, *Colloids Surfaces A Physicochem. Eng. Asp.*, **440**, 197 (2014).
40. I. I. Diakonov, J. Schott, F. Martin, J. C. Harrichourry, and J. Escalier, *Geochim. Cosmochim. Acta*, **63**, 2247 (1999).
41. C. I. Müller, K. Sellschopp, M. Tegel, T. Rauscher, B. Kieback, and L. Röntzsch, *J. Power Sources*, **304**, 196 (2016).
42. A. Maïhatchi, M.-N. Pons, Q. Ricoux, F. Goettmann, and F. Lapicque, *J. Electrochem. Sci. Eng.*, **10**, 95 (2020).